Chemical Science

ROYAL SOCIETY OF CHEMISTRY

EDGE ARTICLE

View Article Online
View Journal | View Issue

Cite this: *Chem. Sci.*, 2024, **15**, 1384

All publication charges for this article have been paid for by the Royal Society of Chemistry

A Ru/RuO_2 heterostructure boosting electrochemistry-assisted selective benzoic acid hydrogenation†

Zifan Cao,[a] Chenhui Wang,[a] Yifan Sun,[a] Menghui Liu,[a] Wei Li,[a] Jinli Zhang *[ab] and Yan Fu *[a]

Received 8th October 2023
Accepted 13th December 2023

DOI: 10.1039/d3sc05312a

rsc.li/chemical-science

Electrocatalytic hydrogenation of benzoic acid (BA) to cyclohexanecarboxylic acid (CCA) at ambient temperature and pressure has been recognized as a promising alternative to thermal hydrogenation since water is required as the hydrogen source. So far, only a few Pt-based electrocatalysts have been developed in acidic electrolyte. To overcome the limitations of reactant solubility and catalyst corrosion, herein, carbon fiber-supported Ru electrocatalysts with abundant Ru/RuO_2 heterojunctions were fabricated *via* cyclic electrodeposition between −0.8 and 1.1 V *vs.* Ag/AgCl. In an alkaline environment, a Ru/RuO_2 catalyst achieves an excellent ECH reactivity in terms of high BA conversion (100%) and selectivity towards CCA (100%) within 180 min at a current density of 200/3 mA cm^{-2}, showing exceptional reusability and long-term stability. 1-Cyclohexenecarboxylic acid (CEA) was identified as the reaction intermediate, whose the selectivity is governed by the applied potential. Kinetic studies demonstrate that ECH of BA over Ru/RuO_2 follows a Langmuir–Hinshelwood (L–H) mechanism. *In situ* Raman spectroscopy and theoretical calculations reveal that the Ru/RuO_2 interface enhances the adsorption strength of CEA, thereby facilitating the production of fully hydrogenated CCA. This work provides a deep understanding of the ECH pathway of BA in alkaline media, and gives a new methodology to fabricate heterostructure electrocatalysts.

Introduction

Cyclohexane carboxylic acid (CCA) is an important organic intermediate for therapeutic drugs, such as ansatrienin, praziquantel and caprolactam,[1,2] and its derivatives are important intermediates for organic synthesis in fine chemical industries, such as *trans*-4-isopropylcyclohexyl acid and cyclohexylmethyl carbamate. For industrial scale synthesis of CCA, selective hydrogenation of benzoic acid (BA) to CCA has attracted growing research attention in the past few years[3–12] (listed in Table S1†). At 80 °C and 1 MPa H_2, Qiu *et al.*[13] realized a CCA selectivity of 100% at a conversion of 89.4% over Ru nanoparticles loaded on N-doped porous two-dimensional carbon nanosheets without hydrogenated intermediates (pathway I as illustrated in Scheme 1). For comparison, Ren *et al.*[14] reported that the Ru/PPh_3@FDU catalyst achieved a CCA selectivity of 98% with 99% conversion at 60 °C and 1 MPa H_2, showing CEA as the reaction intermediate (as shown in Scheme 1). Guo *et al.*[15] fabricated Pt/TiO_2 to achieve BA conversion (90%) with a CCA selectivity of 99% at 80 °C and 50 bar H_2 *via* pathway II (Scheme 1). Moreover, the RhPt/MCM-41 bimetallic catalyst[16] offered a conversion of 63.5% and a selectivity of 97.8% at 40 °C and 1 MPa H_2, following reaction pathway II (Scheme 1). Accordingly, the reaction pathway from BA to CCA is highly dependent upon the feature of the catalyst. Hence, it is urgent to design high-efficiency catalysts with satisfactory conversion.

Electrocatalytic hydrogenation (ECH) of aromatic organics without external H_2 gas has aroused extensive research activities.[17–25] For example, Peng *et al.* employed a ternary PtRhAu electrocatalyst to reach a high faradaic efficiency (58%) toward 2-methoxycyclohexanol from guaiacol.[26] Moreover, Ni–MoO_2 catalysts were designed to perform ECH of phenol to

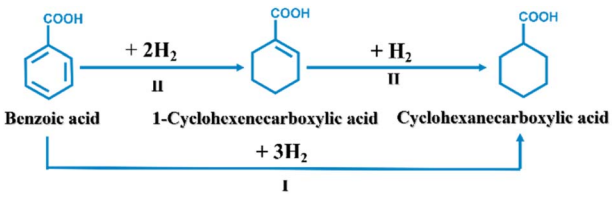

Scheme 1 Reaction pathways for thermal catalytic hydrogenation of BA.

[a]School of Chemical Engineering & Technology, Tianjin University, Tianjin, 300350, China. E-mail: fuyan@tju.edu.cn; zhangjinli@tju.edu.cn
[b]School of Chemistry and Chemical Engineering, Shihezi University, Shihezi, 832003, China

† Electronic supplementary information (ESI) available. See DOI: https://doi.org/10.1039/d3sc05312a

cyclohexanol and cyclohexanone at 60 °C.[27] Recently, several Pt-based electrocatalysts have been used for ECH of BA in an acidic environment.[28] Du *et al.*[29] developed a bimetallic PtRu alloy supported on carbon paper (CP), yielding a conversion of 98.6% with a CCA selectivity of 100%. The PtRu/CP alloy catalyst exhibits significantly higher conversion than that on Pt/CP (51.7%) or Ru/CP (5.8%). Moreover, a coral-shaped PtRu/$Ni(OH)_2$ electrocatalyst simultaneously achieved a 100% conversion of BA along with a 100% selectivity to CCA,[30] significantly outperforming its monometallic counterpart Pt/$Ni(OH)_2$ or Ru/$Ni(OH)_2$. Nevertheless, owing to low solubility of BA in acidic electrolyte as well as acid corrosion of the electrocatalyst, it's highly desirable to develop high-efficiency electrocatalysts for ECH of BA in alkaline media at ambient temperature and pressure.

In this work, self-supporting Ru-based electrocatalysts were *in situ* constructed on activated carbon cloths *via* a cyclic voltammetry electrodeposition technique. Through regulating the electrodeposition potential range, both the loading amount and electronic state can be facilely tuned. An optimal electrocatalyst with abundant Ru/RuO_2 heterostructures exhibits unprecedented performance for ECH of BA in alkaline electrolyte. BA conversion and CCA selectivity are both greatly associated with the applied potential and KOH concentration. The ECH mechanism and the indispensable role of the Ru/RuO_2 interface were revealed by the kinetic study, *in situ* spectroelectrochemical technique and theoretical calculations.

Results and discussion

Cyclic electrodeposition enables the formation of a Ru/RuO_2 heterostructure

A series of Ru/CC electrode materials were synthesized *via* CV electrodeposition with various potential ranges as illustrated in Scheme 2. According to CV profiles during electrodeposition (Fig. S1†), there are four potentials at which an increase in deposition current can be observed in the cathodic scan: (i) the peak 'A' at 0.74 V *vs.* Ag/AgCl corresponding to the reduction of Ru^{3+} to metallic Ru ($Ru^{3+} + 3e^- \rightleftharpoons Ru$, $E = 0.74$ V *vs.* Ag/AgCl);[31] (ii) the peak 'B' observed at around 0.30–0.45 V *vs.* Ag/AgCl reflecting the potential range for underpotential-deposited hydrogen (UPD H) adsorption; (iii) the peak 'C' at −0.4 V *vs.* Ag/AgCl denoting the H absorption;[32] (iv) the peak 'F' attributable to H_2 evolution.[33] During the subsequent anodic scan, 'G' corresponds to H_2 oxidation, the peak 'D' appears due to H_{abs} desorption, the peak 'E' means H_{UPD} desorption, and 'H' indicates the oxidation of Ru^{3+} to Ru^{4+}.[34]

According to SEM and TEM images, it can be clearly seen that densely packed Ru particles uniformly cover the surface of CC when the electrodeposition potential lies in the range of −0.8 to 1.1 V *vs.* Ag/AgCl (Fig. 1a and S2a†). For comparison, the above-mentioned range is separated into relatively low potential (−0.8 to 0 V) and relatively high potential (0–1.1 V), respectively. Consequently, some large aggregates are observed on the deposited metal layer within either the low potential range (Fig. 1b and S2b†) or the high potential range (Fig. 1c and S2c†). As the potential moves negatively to −1.0 to 0.9 V and −1.3 to 0.6 V, the deposited metal species agglomerate significantly and disperse unevenly (Fig. S3 and S4†). As the potential changes

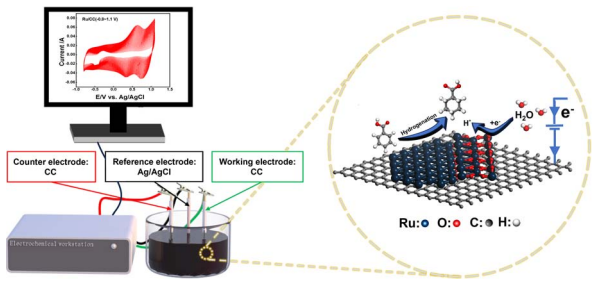

Scheme 2 Schematic illustration for synthesis of Ru/CC (−0.8 to 1.1 V) *via* cyclic electrodeposition.

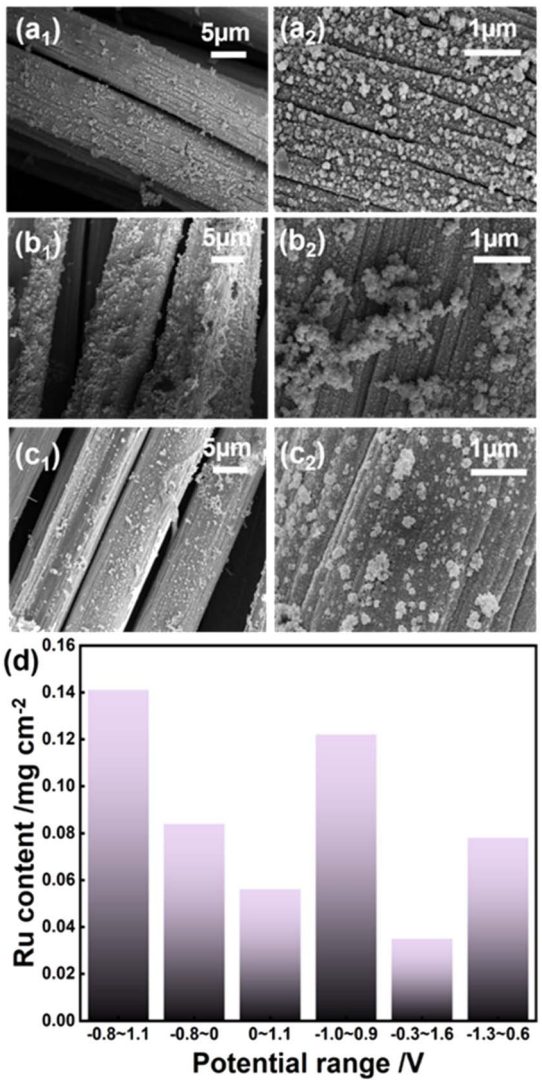

Fig. 1 SEM images of (a) Ru/CC (−0.8 to 1.1 V), (b) Ru/CC (−0.8 to 0 V), and (c) Ru/CC (0–1.1 V). (d) The mass loading of Ru for Ru/CC (−0.8 to 1.1 V), Ru/CC (−0.8 to 0 V), Ru/CC (0–1.1 V), Ru/CC (−1.0 to 0.9 V), Ru/CC (−0.3 to 1.6 V) and Ru/CC (−1.3 to 0.6 V).

positively to −0.3 to 1.6 V, fewer deposits can be detected as compared to those obtained with more negative potentials.

The loading amounts of Ru prepared with different potential ranges were determined by ICP-OES. As shown in Fig. 1d, Ru/CC (−0.8 to 1.1 V) shows the maximum loading mass while Ru/CC (−0.3 to 1.6 V) exhibits the minimum content. Ru/CC (−0.8 to 1.1 V) contains 0.141 mg cm^{-2} of Ru species, which is significantly higher relative to 0.0812 mg cm^{-2} for Ru/CC (−0.8 to 0 V) and 0.0567 mg cm^{-2} for Ru/CC (0–1.1 V). Nevertheless, as the potential range moves negatively, the Ru content gradually decreases to 0.122 mg cm^{-2} for Ru/CC (−1.0 to 0.9 V) and 0.0787 mg cm^{-2} for Ru/CC (−1.3 to 0.6 V). Hence, an evenly distributed metal layer can form within a suitable potential range. The crystalline structures of different Ru electrode materials were analyzed by HRTEM. Interestingly, the Ru/RuO_2 heterointerface for Ru/CC (−0.8 to 1.1 V) was analyzed through interplanar spacing in HRTEM and the fast Fourier transform (FFT) diffraction pattern (shown in Fig. 2a). The interplanar spacing at the interface is different from that of Ru (101) or RuO_2 (210) at the edge. Two kinds of symmetries can be observed from FFT patterns (inset of Fig. 2a), verifying the coexistence of Ru (101) and RuO_2 (210). The tetragonal symmetry could be attributed to RuO_2,[35] and the lattice fringe (d = 0.217 nm) with an angle of 90° represents the (210) plane of RuO_2 (Fig. 2b). A lattice spacing of 0.208 nm with an angle of 60° corresponds well to the (101) plane of metallic Ru (Fig. 2c).[36]

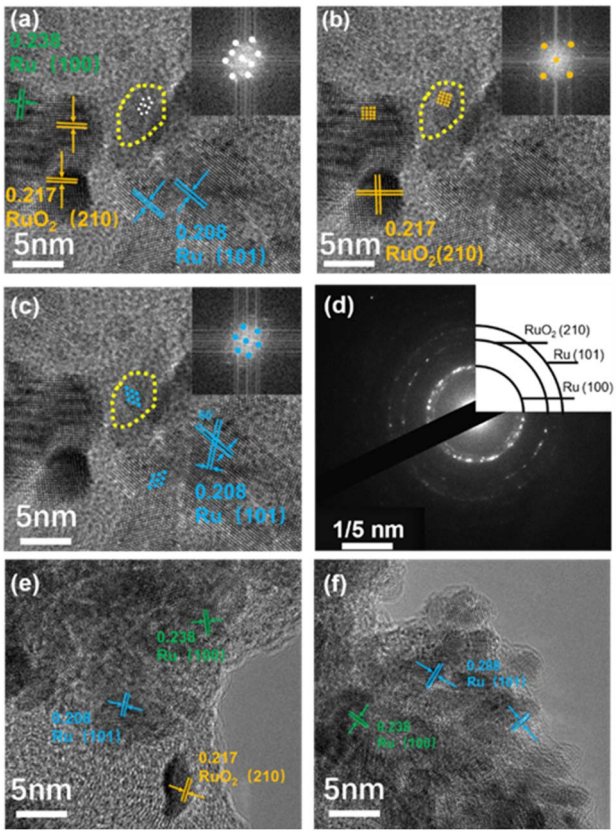

Fig. 2 (a–c) HRTEM images of Ru/CC (−0.8 to 1.1 V) and the corresponding FFT patterns. (d) SAED pattern of Ru/CC (−0.8 to 1.1 V). HRTEM images of (e) Ru/CC (0–1.1 V) and (f) Ru/CC (−0.8 to 0 V).

Notably, the lattice fringes of Ru and RuO_2 fuse together at the interface. For comparison, identical patterns can be observed around the interface, which are consistent with Ru and RuO_2 (Fig. 2b and c). So, it can be reasonably deduced that the Ru/RuO_2 interface has a distinctive structure with Ru (101)/RuO_2 (210) intercalation. The corresponding SAED pattern further confirms that the strongest orientations for Ru and RuO_2 are indexed to the (101) and (210) crystal planes, respectively (Fig. 2d). Moreover, Ru/CC (0–1.1 V) exhibits characteristic crystal planes of Ru (101), Ru (100) and RuO_2 (210), whereas Ru/CC (−0.8 to 0 V) displays typical lattice fringes for Ru (101) and Ru (100) (Fig. 2e and f). The corresponding SAED patterns verify the HRTEM analysis (Fig. S5†). The element mapping confirms the uniform distribution of Ru species (Fig. S6†).

The electronic states of the as-synthesized electrode materials were characterized by XPS (Fig. 3 and S7 and Table S2†). Except for Ru/CC (−0.8 to 0 V), all the Ru electrocatalysts are composed of metallic Ru^0 atoms and high valent Ru^{4+} species, which are in perfect agreement with HRTEM analysis. The deconvolution spectra of Ru 3p for Ru/CC (−0.8 to 1.1 V) present two typical peaks at the binding energies (B.E.s) of 461.88 and 484.08 eV, respectively, which are ascribed to Ru^0 $3p_{3/2}$ and Ru^0 $3p_{1/2}$.[37] The B.E.s located at 464.38 and 486.48 eV are attributable to Ru^{4+} $3p_{3/2}$ and Ru^{4+} $3p_{1/2}$ respectively, indicating the existence of RuO_2.[38] Accordingly, Ru/CC (−0.8 to 1.1 V) possesses 68.13% of Ru^0 along with 31.87% of RuO_2. As the potential range shifts negatively, the relative proportion of Ru^0 apparently increases (see Table S2†). Ru/CC (−0.8 to 0 V) is composed of metallic Ru^0 atoms with the B.E.s at 461.58 and 483.88 eV, respectively. As a control, Ru/CC (0–1.1 V) exhibits two valence states involving Ru^0 (64.26%) and Ru^{4+} (35.74%). Overall, the loading mass, dispersity and electronic state of Ru species are greatly associated with electrodeposition potential ranges.

Ru/RuO_2 promotes electrocatalytic hydrogenation of BA

First, the effects of applied potentials were investigated under the same passed charges (Fig. 4a). Within various potentials, CEA is the only intermediate product during ECH of BA. At 0 V *vs.* RHE, the conversion of BA is close to 17.6%, and the hydrogenated products contain 19.6% of CCA and 80.4% of CEA. As the potential drops to −0.1 V *vs.* RHE, either the conversion of BA or the selectivity of CCA shows a sudden increase. With the applied potential stepping from −0.1 to −0.4 V *vs.* RHE, both the conversion of BA and the selectivity of CCA exhibit gradual enhancement. At −0.4 V *vs.* RHE, a selectivity of 82.5% is realized toward CCA at a conversion of 75.7%. With the potential changing to −0.5 V *vs.* RHE, the conversion of BA slightly decreases to 69%. Next, five cycles of ECH at −0.2 V *vs.* RHE were performed. As a consequence, ECH of BA maintains a faradaic efficiency of around 47% (Fig. 4b), indicating that Ru/CC (−0.8 to 1.1 V) possesses high stability toward CCA production.

Notably, Ru-based electrode materials exhibit distinct ECH performance with different electrodeposition potential ranges (Fig. 5a). For Ru/CC (−0.8 to 1.1 V), the conversion reaches 95.8% after 120 min at 200/3 mA cm^{-2}, giving a selectivity of 95.2% toward CCA. The catholyte after 30 min of ECH was analyzed by GC-MS (Fig. S8–S10†). It is demonstrated that the only reaction intermediate is CEA. Under the same electrolysis

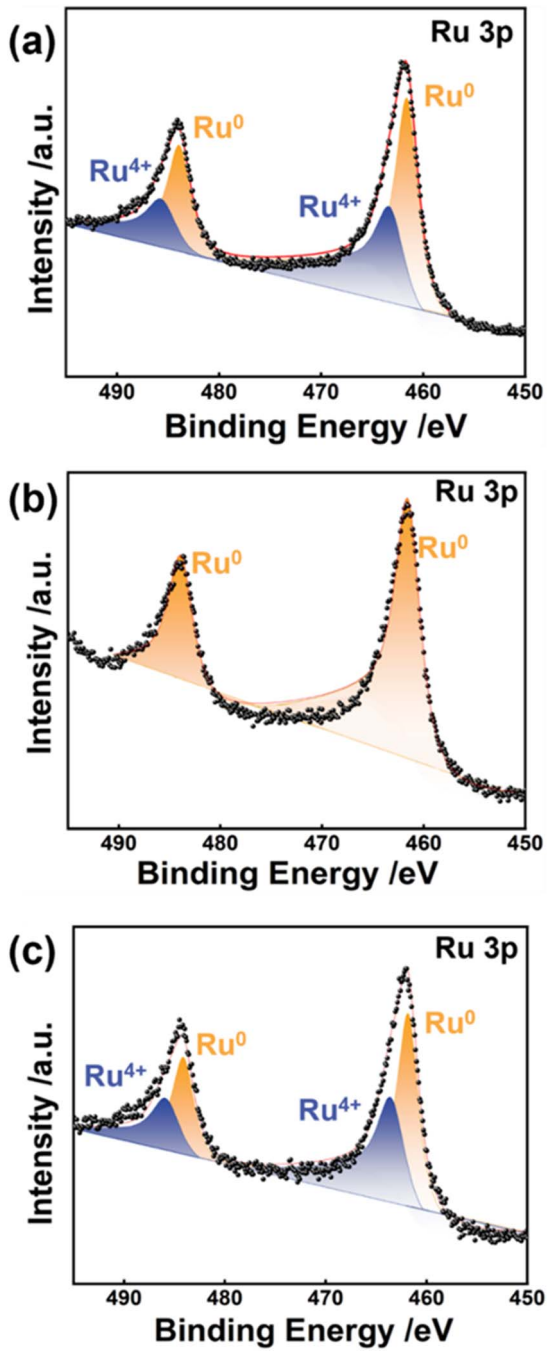

Fig. 3 Ru 3p XPS spectra of (a) Ru/CC (−0.8 to 1.1 V), (b) Ru/CC (−0.8 to 0 V), and (c) Ru/CC (0–1.1 V).

conditions, Ru/CC (−0.8 to 0 V) and Ru/CC (0–1.1 V) show a conversion of 22.5% and 33.2%, respectively, accompanied by a certain proportion of CEA. Additionally, Ru/CC (−1.0 to 0.9 V) shows a conversion of 61.6%, whereas Ru/CC (−0.3 to 1.6 V) and Ru/CC (−1.3 to 0.6 V) exhibit extremely low activity for ECH of BA. So, it can be assumed that different ECH performances may be attributable to various electrodeposition potential ranges, which affect the loading mass, dispersity and electronic state of Ru species.[39]

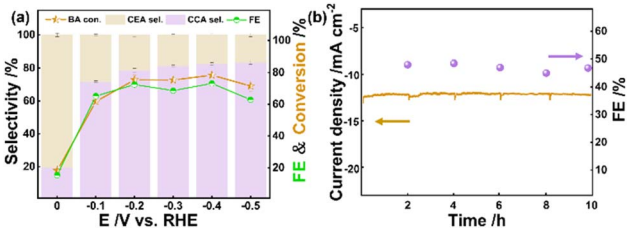

Fig. 4 (a) The catalytic performance of Ru/CC (−0.8 to 1.1 V) at different applied potentials in 0.1 M KOH with 110 C of charges passed. (b) The faradaic efficiency and current density during 10 h of ECH at −0.2 V *vs.* RHE; the electrolyte was refreshed every 2 h.

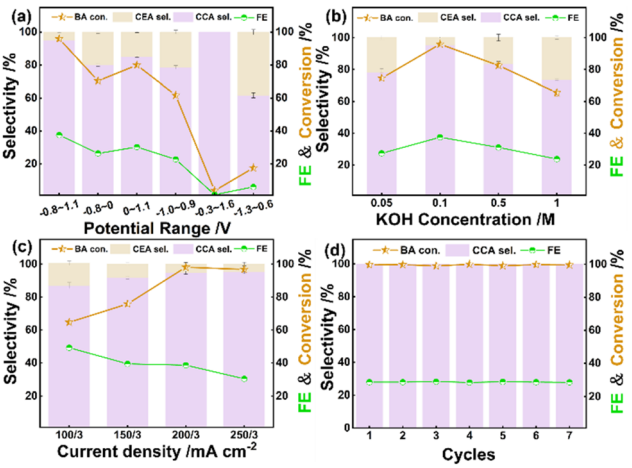

Fig. 5 (a) ECH of BA over the as-synthesized catalysts at a current density of 200/3 mA cm^{-2}; the reaction time is 120 min. (b) the conversion, FE and selectivity over Ru/CC (−0.8 to 1.1 V) at 200/3 mA cm^{-2} with different concentrations of KOH; the concentration of BA is 50 mM, and the reaction time is 120 min. (c) The conversion, FE and selectivity over Ru/CC (−0.8 to 1.1 V) at different current densities; the reaction time is 120 min. (d) Stability test over Ru/CC (−0.8 to 1.1 V) at 200/3 mA cm^{-2}; the reaction time is 180 min. The concentration of BA is 50 mM for all the tests.

Considering the concentration of electrolyte, it should be noted that ECH of BA achieves the optimal performance in 0.1 M KOH (Fig. 5b). The influence of current density and reaction time was further studied to optimize the electrolysis conditions (Fig. 5c and S11†). At 100/3 mA cm^{-2}, the conversion comes up to 100% within 600 min while the selectivity gradually increases from 62.0% to 100%. Apparently, the total reaction time significantly decreases to 180 min when the current density increases from 100/3 mA cm^{-2} to 200/3 mA cm^{-2}. At 250/3 mA cm^{-2}, it takes a longer time to reach a conversion of 100% relative to that at 200/3 mA cm^{-2}. This implies the fierce competition of the HER at large current density. The effect of reagent concentration was investigated at 200/3 mA cm^{-2} (Fig. S12†). It takes 120 min to accomplish 100% conversion for 40 mM BA. The total reaction time extends to 480 min for 80 mM BA.

Furthermore, we also employed 0.05 M H_2SO_4, 0.1 M NaOH, 0.1 M Na_2CO_3 and 0.1 M $NaHCO_3$ as the control electrolytes. Owing to the poor solubility of BA in H_2SO_4 solution, we used

relatively low concentration of BA (5 mM). As can be seen in Fig. S13 and Table S3,† the conversion of BA reaches 91.67% at 180 min in acidic media, giving 100% selectivity toward CCA. In NaOH electrolyte, the conversion reaches 93.3% with a CCA selectivity of 95.65%, which is a little lower than that in KOH electrolyte. Moreover, ECH of BA in Na_2CO_3 and $NaHCO_3$ achieves the conversions of 80.0% and 82.3%, respectively, accompanied by small fractions of CEA. Considering the influence of the aromatic ring structure of benzoic acid derivatives, ECH of *p*-methyl benzoic acid was studied at 200/3 mA cm^{-2} in 0.1 M KOH. As a consequence, a conversion of 83.3% was achieved at 10 h with 100% selectivity toward 4-methyl cyclohexane carboxylic acid. Clearly, ECH of *p*-methyl benzoic acid is more time-consuming than that of BA. Future studies will focus on the investigation of the catalytic mechanism and the optimization of electrocatalysts for broad benzoic acid derivatives.

HRTEM and XPS analysis demonstrate that Ru/CC (−0.8 to 1.1 V) is composed of two phases (Ru and RuO_2) while Ru (−0.8 to 0 V) only contains metallic Ru^0 species. To elucidate the role of the Ru/RuO_2 heterostructure, two catalysts involving Ru/CC (−0.8 to 1.1 V) with 100 CV cycles and Ru (−0.8 to 0 V) with 225 CV cycles were compared at the same current density. To ensure the same electrodeposition time as that of Ru/CC (−0.8 to 1.1 V), the number of CV cycles was increased to 225 for Ru/CC (−0.8 to 0 V). It is also worth noting that the selectivity toward CEA changes slightly on prolonging the reaction time (Fig. S14†), which indicates that full hydrogenation of BA proceeds slowly over Ru/CC (−0.8 to 0 V). For comparison, 100% selectivity toward CCA is rapidly realized over Ru/CC (−0.8 to 1.1 V) (Fig. S11c†). For ECH of CEA, Ru/CC (−0.8 to 1.1 V) also exhibits much higher activity as compared to Ru/CC (−0.8 to 0 V) (Fig. S15†). Accordingly, it can be reasonably deduced that Ru/CC (−0.8 to 1.1 V) embedded with Ru/RuO_2 heterointerfaces facilitates ECH of BA into CCA.

The stability test for Ru/CC (−0.8 to 1.1 V) was conducted at 200/3 mA cm^{-2} *via* seven cycles of ECH, in which each cycle proceeds for 180 min. As can be seen in Fig. 5d, Ru/CC (−0.8 to 1.1 V) maintains outstanding performance without apparent loss of activity. The spent Ru/CC (−0.8 to 1.1 V) shows identical surface morphology, Ru loading mass (0.138 mg cm^{-2}) and valence distribution (Ru^0 accounts for 63.5%) (Fig. S16–S18†) to the as-synthesized sample. So, it is demonstrated that Ru/CC (−0.8 to 1.1 V) possesses outstanding durability during ECH of BA in alkaline electrolyte.

Mechanism study for ECH of BA

According to LSV profiles of Ru-based catalysts (Fig. S19, Table S4†), it can be found that Ru/CC (−0.8 to 1.1 V) shows a minimum overpotential (η_{10}) of ∼110 mV with 50 mM BA added, which implies that electrochemical reduction of BA is kinetically favorable on Ru/CC (−0.8 to 1.1 V). What's more, addition of BA increases the overpotential of the Ru-based electrocatalyst, indicating that adsorption of BA on the electrode surface hinders hydrogen adsorption and evolution.[40,41] As shown in Fig. 6a, Ru/CC (−0.8 to 1.1 V) exhibits the smallest Tafel slope of 176 mV dec^{-1}, which signifies the best performance for ECH of BA. Electrochemical impedance was employed to demonstrate the electron transfer efficiency of the catalysts (Fig. 6b). Ru/CC (−0.8 to 1.1 V) shows the smallest R_{ct} (21 Ω cm^{-2}) among the investigated samples, suggesting the most efficient electron transfer between the electrode and electrolyte.

Without BA added, the CV curve of Ru/CC (−0.8 to 1.1 V) exhibits a shoulder wave at around 0.1 V *vs.* RHE in the cathodic scan as well as a distinct peak at 0.2 V *vs.* RHE in the anodic scan, which can be attributed to H* adsorption and desorption. On increasing the concentration of BA, both cathodic and anodic currents progressively decrease owing to competitive adsorption between H_2O and BA (Fig. 6c).[42] To unveil the reaction mechanism, reaction rates were assessed at different initial concentrations of BA. As a result, a negative reaction order of −1.02 was obtained for ECH of BA in 0.1 M KOH over Ru/CC (−0.8 to 1.1 V), which is indicative of a Langmuir–Hinshelwood (L–H) mechanism (Fig. 6d).[43–45] Combined with the CV results, it is indicated that ECH of BA consumes active H* on the catalyst surface.

To further explore the reaction mechanism, *in situ* Raman spectroscopy was performed with different applied potentials. As shown in Fig. 7a, Raman spectra collected for negatively charged BA on the catalyst surface exhibit three distinguishable peaks:[46,47] (i) aromatic ring vibration $\nu(C–C)_{ring}$ at 1600 cm^{-1}, (ii) carboxylate group vibration $\nu(COO^-)_{sym}$ at 1350 and 1390 cm^{-1}, (iii) ring breathing at 1005 cm^{-1}. On applying positive potentials (0.1–0.2 V), the above-mentioned typical peaks are intensified on the catalyst surface, which implies that a positive potential enhances the adsorption strength of a negatively charged reactant. It is worth noting that the intensities of these typical bands are greatly weakened at 0 V *vs.* RHE. Combined with ECH performance (see Fig. 4a), the decreased signal could be explained by the hydrogenation of benzoate. Moreover, these

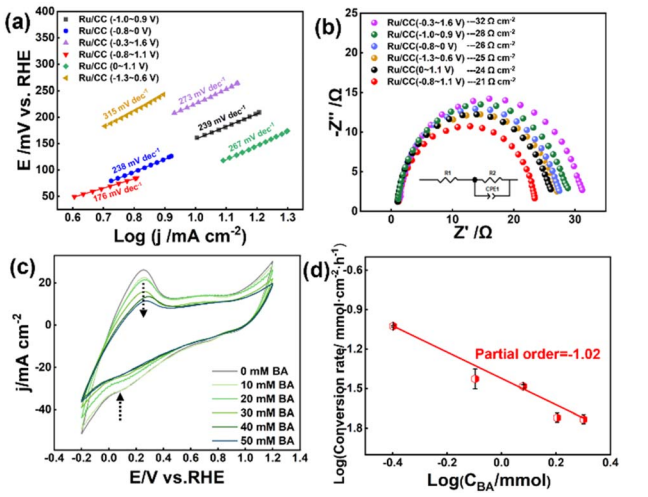

Fig. 6 (a) Tafel slopes and (b) Nyquist plots of Ru/CC (−0.8 to 1.1 V), Ru/CC (−0.8 to 0 V), Ru/CC (0–1.1 V), Ru/CC (−1.0 to 0.9 V), Ru/CC (−1.3 to 0.6 V) and Ru/CC (−0.3 to 1.6 V). (c) CV curves of Ru/CC (−0.8 to 1.1 V) with different concentrations of BA. (d) Kinetic study for ECH of BA over Ru/CC (−0.8 to 1.1 V); the conversion of BA is controlled less than 15%.

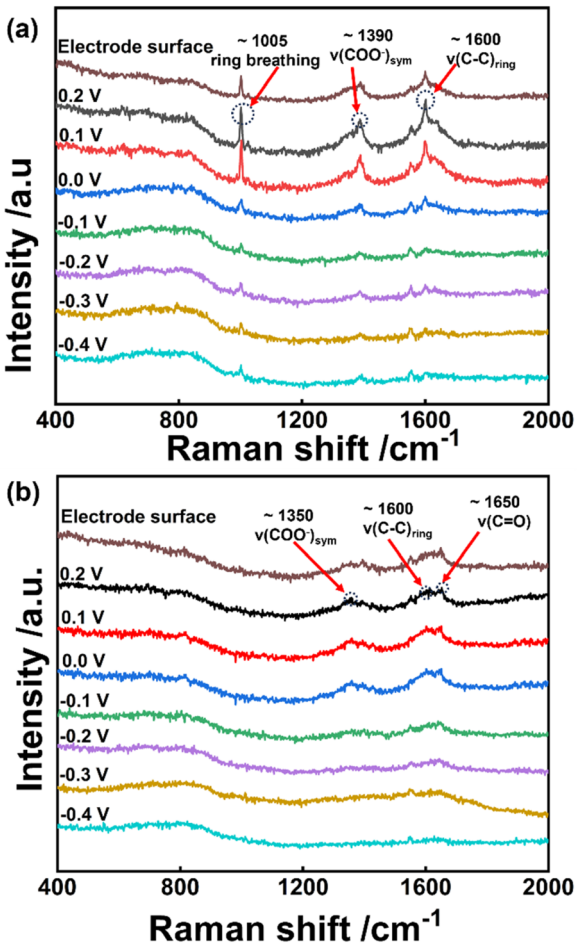

Fig. 7 *In situ* Raman spectra collected on the Ru/CC (−0.8 to 1.1 V) surface for (a) benzoate and (b) cyclohexene carboxylate in 0.1 M KOH at different applied potentials.

peaks almost remain unchanged within −0.1 to −0.4 V. To further explore the effect of applied potentials, *in situ* Raman spectroscopy was performed on non-catalytic carbon cloth (Fig. S20†). The typical peaks basically remain unchanged in the potential range of 0.2 to −0.4 V. This implies that the peak intensity will not decrease significantly if no reaction occurs. For comparison, the characteristic bands for cyclohexene carboxylate show a sudden decrease at −0.1 V, and gradually descend as the potential negatively shifts from −0.1 to −0.4 V (Fig. 7b). So, it is indicated that the hydrogenation of cyclohexene carboxylate requires a more negative potential than that of benzoate.

To further reveal the role of the Ru/RuO_2 heterostructure during ECH, the adsorption energies of potassium benzoate and potassium cyclohexene carboxylate were calculated on the Ru (101)/RuO_2 (210) model (Fig. 8a, b, S21 and S22†). As shown in Fig. 8a, potassium benzoate adsorbing on the Ru (101) surface of the heterostructure model ($*Ru/RuO_2$) exhibits a superior adsorption energy of −3.57 eV, followed by the figures for interface and Ru/RuO_2^* sites (−2.24 eV in comparison with −2.41 eV). Fig. 8b demonstrates that the adsorption energy of potassium cyclohexene carboxylate on the interface

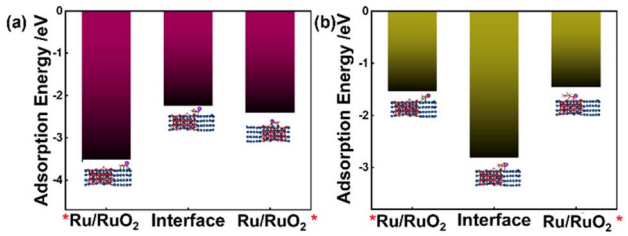

Fig. 8 Adsorption energy of (a) potassium benzoate and (b) potassium cyclohexene carboxylate on different sites of the Ru (101)/RuO_2 (210) model.

(−2.81 eV) is much larger than that on $*Ru/RuO_2$ (−1.53 eV) or Ru/RuO_2^* (−1.45 eV). It is noteworthy that the adsorption energy of potassium cyclohexane carboxylate on the interface is only −0.57 eV (Fig. S23†), which is much smaller than that of potassium cyclohexene carboxylate (−2.81 eV). Accordingly, the Ru site facilitates the adsorption of potassium benzoate while the interface promotes the adsorption of potassium cyclohexene carboxylate. DFT calculations reveal that the critical role of the Ru/RuO_2 heterointerface is to promote the adsorption strength of the intermediate potassium cyclohexene carboxylate, which is in accordance with ECH results (Fig. S15†).

Conclusion

A facile CV electrodeposition was adopted to fabricate self-supporting Ru-based electrocatalysts on activated carbon cloths through regulating the potential ranges. Both the loading amount and electronic state can be facilely tuned. The optimal electrocatalyst with abundant Ru/RuO_2 heterostructures exhibits unprecedented performance for ECH of BA in alkaline electrolyte. In an alkaline environment, the Ru/RuO_2 catalyst achieves high BA conversion (100%) and selectivity towards CCA (100%) within 180 min at 200/3 mA cm^{-2}, showing excellent reusability and long-term stability. 1-Cyclohexenecarboxylic acid (CEA) was identified as the reaction intermediate, whose the selectivity is governed by the applied potential. Kinetic studies demonstrate that ECH of BA over Ru/RuO_2 follows a Langmuir–Hinshelwood (L–H) mechanism. *In situ* Raman spectroscopy and theoretical calculations unravel that the Ru/RuO_2 interface enhances the adsorption strength of cyclohexene carboxylate, thereby facilitating the production of fully hydrogenated cyclohexane carboxylate. This work provides a deep understanding of the ECH pathway of BA in alkaline media and gives a new methodology to fabricate heterostructure electrocatalysts.

Author contributions

Zifan Cao carried out the synthesis and characterization, performed electrochemical experiments and wrote the paper; Chenhui Wang undertook DFT calculations for the article; Yifan Sun and Menghui Liu assisted with electrocatalytic experiments and participated in discussion; Wei Li and Jinli Zhang acquired funding; Yan Fu conceived the project and supervised the work.

All authors have approved the published version of the manuscript.

Conflicts of interest

The authors declare that they have no known competing financial interests or personal relationships that could have appeared to influence the work reported in this paper.

Acknowledgements

This study was funded by the National Natural Science Foundation of China (21878225).

Notes and references

1 B. S. Moore, H. Cho, R. Casati, E. Kennedy, K. A. Reynolds, U. Mocek, J. M. Beale and H. G. Floss, Biosynthetic studies on ansatrienin A. Formation of the cyclohexanecarboxylic acid moiety, *J. Am. Chem. Soc.*, 1993, **115**, 5254–5266.

2 H. Shinkai, M. Nishikawa, Y. Sato, K. Toi, I. Kumashiro, Y. Seto, M. Fukuma, K. Dan and S. Toyoshima, N-(Cyclohexylcarbonyl)-D-phenylalanines and related compounds. A new class of oral hypoglycemic agents. 2, *J. Med. Chem.*, 1989, **32**, 1436–1441.

3 Y. Hu, W. Chen, Y. Chen, F. Zhang, W. Song, L. Wang, J. Fu, X. Ren, S. You, C. Cao, Z. Yu and X. Dong, Highly Effective $Rh/NaNbO_3$ Catalyst for the Selective Hydrogenation of Benzoic Acid to Cyclohexane Carboxylic Acid Under Mild Conditions, *Catal. Lett.*, 2022, **152**, 2164–2177.

4 X. Wen, Y. Cao, X. Qiao, L. Niu, L. Huo and G. Bai, Significant effect of base on the improvement of selectivity in the hydrogenation of benzoic acid over NiZrB amorphous alloy supported on γ-Al_2O_3, *Catal. Sci. Technol.*, 2015, **5**, 3281–3287.

5 W. Lian, B. Chen, B. Xu, S. Zhang, Z. Wan, D. Zhao, N. Zhang and C. Chen, Acquiring Clean and Highly Dispersed Nickel Particles (*ca.* 2.8 nm) by Growing Nickel-Based Nanosheets on Al_2O_3 as Efficient and Stable Catalysts for Harvesting Cyclohexane Carboxylic Acid from the Hydrogenation of Benzoic Acid, *Ind. Eng. Chem. Res.*, 2019, **58**, 2846–2856.

6 H. Zhang, G. Li, R. Nie, X. Lu and Q. Xia, One-pot synthesized mesoporous C-TiO_2 hybrid for Ru-catalyzed low-temperature hydrogenation of benzoic acid, *J. Mater. Sci.*, 2019, **54**, 7529–7540.

7 Z. Jiang, G. Lan, X. Liu, H. Tang and Y. Li, Solid state synthesis of Ru–MC with highly dispersed semi-embedded ruthenium nanoparticles in a porous carbon framework for benzoic acid hydrogenation, *Catal. Sci. Technol.*, 2016, **6**, 7259–7266.

8 X. Xu, M. Tang, M. Li, H. Li and Y. Wang, Hydrogenation of Benzoic Acid and Derivatives over Pd Nanoparticles Supported on N-Doped Carbon Derived from Glucosamine Hydrochloride, *ACS Catal.*, 2014, **4**, 3132–3135.

9 C. Chaudhari, H. Imatome, Y. Nishida, K. Sato and K. Nagaoka, Recyclable Rh-PVP nanoparticles catalyzed hydrogenation of benzoic acid derivatives and quinolines under solvent-free conditions, *Catal. Commun.*, 2019, **126**, 55–60.

10 H. Zhang, J. Dong, X. Qiao, J. Qin, H. Sun, A. Wang, L. Niu and G. Bai, *In situ* generated highly dispersed nickel nanoclusters confined in MgAl mixed metal oxide platelets for benzoic acid hydrogenation, *J. Catal.*, 2019, **372**, 258–265.

11 X. H. Lu, Y. Shen, J. He, R. Jing, P. P. Tao, A. Hu, R. F. Nie, D. Zhou and Q. H. Xia, Selective hydrogenation of benzoic acid to cyclohexane carboxylic acid over microwave-activated Ni/carbon catalysts, *Mol. Catal.*, 2018, **444**, 53–61.

12 A. Fukazawa, Y. Shimizu, N. Shida and M. Atobe, Electrocatalytic hydrogenation of benzoic acids in a proton-exchange membrane reactor, *Org. Biomol. Chem.*, 2021, **19**, 7363–7368.

13 Z. Qiu, S. Ma, X. He, Z. Li, Z. Xiong, Y. Cao and G. Li, Nitrogen-Doped Porous Two-dimensional Carbon Nanosheets Derived from ZIF-8 as Multifunctional Supports of Ru Nanoparticles for Hydrogenation of Benzoic Acid, *Catal. Lett.*, 2023, **153**, 388–397.

14 X. Ren, M. Guo, H. Li, C. Li, L. Yu, J. Liu and Q. Yang, Microenvironment Engineering of Ruthenium Nanoparticles Incorporated into Silica Nanoreactors for Enhanced Hydrogenations, *Angew. Chem., Int. Ed.*, 2019, **58**, 14483–14488.

15 M. Guo, X. Kong, C. Li and Q. Yang, Hydrogenation of benzoic acid derivatives over Pt/TiO_2 under mild conditions, *Commun. Chem.*, 2021, **4**, 54.

16 M. Wang, M. Guo, X. Ren, X. Liu and Q. Yang, The Influence of Surface Structure of RhPt Bimetallic Nanoparticles on the Hydrogenation of Aromatic Compounds, *J. Phys. Chem. C*, 2021, **125**, 15275–15282.

17 K. Koh, U. Sanyal, M.-S. Lee, G. Cheng, M. Song, V.-A. Glezakou, Y. Liu, D. Li, R. Rousseau, O. Y. Gutiérrez, A. Karkamkar, M. Derewinski and J. A. Lercher, Electrochemically Tunable Proton-Coupled Electron Transfer in Pd-Catalyzed Benzaldehyde Hydrogenation, *Angew. Chem., Int. Ed.*, 2020, **59**, 1501–1505.

18 S. Li, X. Sun, Z. Yao, X. Zhong, Y. Cao, Y. Liang, Z. Wei, S. Deng, G. Zhuang, X. Li and J. Wang, Biomass Valorization *via* Paired Electrosynthesis Over Vanadium Nitride-Based Electrocatalysts, *Adv. Funct. Mater.*, 2019, **29**, 1904780.

19 Y. P. Wijaya, T. Grossmann-Neuhaeusler, R. D. Dhewangga Putra, K. J. Smith, C. S. Kim and E. L. Gyenge, Electrocatalytic Hydrogenation of Guaiacol in Diverse Electrolytes Using a Stirred Slurry Reactor, *ChemSusChem*, 2020, **13**, 629–639.

20 Y. Zhou, Y. Gao, X. Zhong, W. Jiang, Y. Liang, P. Niu, M. Li, G. Zhuang, X. Li and J. Wang, Electrocatalytic Upgrading of Lignin-Derived Bio-Oil Based on Surface-Engineered PtNiB Nanostructure, *Adv. Funct. Mater.*, 2019, **29**, 1807651.

21 P. Nilges and U. Schröder, Electrochemistry for biofuel generation: production of furans by electrocatalytic hydrogenation of furfurals, *Energy Environ. Sci.*, 2013, **6**, 2925–2931.

22 C. J. Bondue and M. T. M. Koper, A mechanistic investigation on the electrocatalytic reduction of aliphatic ketones at platinum, *J. Catal.*, 2019, **369**, 302–311.
23 Q. Gao, T. Mou, S. Liu, G. Johnson, X. Han, Z. Yan, M. Ji, Q. He, S. Zhang, H. Xin and H. Zhu, Monodisperse PdSn/SnOx core/shell nanoparticles with superior electrocatalytic ethanol oxidation performance, *J. Mater. Chem. A*, 2020, **8**, 20931–20938.
24 H. Zhang, S. Wu, X. Huang, L. Li, Q. Liao and Z. Wei, Integrating H2O2 generation from electrochemical oxygen reduction with the selective oxidation of organics in a dual-membrane reactor, *Chem. Eng. J.*, 2022, **428**, 131534.
25 Z. Zhou, L. Zeng, G. Xiong, L. Yang, H. Yuan, J. Yu, S. Xu, D. Wang, X. Zhang, H. Liu and W. Zhou, Multifunctional electrocatalyst of NiCo-NiCoP nanoparticles embedded into P-doped carbon nanotubes for energy-saving hydrogen production and upgraded conversion of formaldehyde, *Chem. Eng. J.*, 2021, **426**, 129214.
26 T. Peng, T. Zhuang, Y. Yan, J. Qian, G. R. Dick, J. Behaghel de Bueren, S.-F. Hung, Y. Zhang, Z. Wang, J. Wicks, F. P. Garcia de Arquer, J. Abed, N. Wang, A. Sedighian Rasouli, G. Lee, M. Wang, D. He, Z. Wang, Z. Liang, L. Song, X. Wang, B. Chen, A. Ozden, Y. Lum, W. R. Leow, M. Luo, D. M. Meira, A. H. Ip, J. S. Luterbacher, W. Zhao and E. H. Sargent, Ternary Alloys Enable Efficient Production of Methoxylated Chemicals *via* Selective Electrocatalytic Hydrogenation of Lignin Monomers, *J. Am. Chem. Soc.*, 2021, **143**, 17226–17235.
27 P. Zhou, S.-X. Guo, L. Li, T. Ueda, Y. Nishiwaki, L. Huang, Z. Zhang and J. Zhang, Selective Electrochemical Hydrogenation of Phenol with Earth-abundant Ni-MoO_2 Heterostructured Catalysts: Effect of Oxygen Vacancy on Product Selectivity, *Angew. Chem., Int. Ed.*, 2023, **62**, e202214881.
28 A. Kong, M. Liu, H. Zhang, Z. Cao, J. Zhang, W. Li, Y. Han and Y. Fu, Highly selective electrocatalytic hydrogenation of benzoic acid over Pt/C catalyst supported on carbon fiber, *Chem. Eng. J.*, 2022, **445**, 136719.
29 Y. Du, X. Chen, W. Shen, H. Liu, M. Fang, J. Liu and C. Liang, Electrocatalysis as an efficient alternative to thermal catalysis over PtRu bimetallic catalysts for hydrogenation of benzoic acid derivatives, *Green Chem.*, 2023, **25**, 5489–5500.
30 M. Liu, C. Wang, Z. Cao, A. Kong, Y. Gao, J. Zhang, Y. Han, W. Li and Y. Fu, Coral-shaped PtRu/$Ni(OH)_2$ electrocatalyst promotes selective hydrogenation of benzoic acid, *Catal. Sci. Technol.*, 2023, **13**, 3568–3578.
31 Q. Zhang, K. Kusada, D. Wu, N. Ogiwara, T. Yamamoto, T. Toriyama, S. Matsumura, S. Kawaguchi, Y. Kubota, T. Honma and H. Kitagawa, Solid-solution alloy nanoparticles of a combination of immiscible Au and Ru with a large gap of reduction potential and their enhanced oxygen evolution reaction performance, *Chem. Sci.*, 2019, **10**, 5133–5137.
32 S. Nogami, N. Shida, S. Iguchi, K. Nagasawa, H. Inoue, I. Yamanaka, S. Mitsushima and M. Atobe, Mechanistic Insights into the Electrocatalytic Hydrogenation of Alkynes on Pt–Pd Electrocatalysts in a Proton-Exchange Membrane Reactor, *ACS Catal.*, 2022, **12**, 5430–5440.
33 A. Zalineeva, S. Baranton, C. Coutanceau and G. Jerkiewicz, Electrochemical Behavior of Unsupported Shaped Palladium Nanoparticles, *Langmuir*, 2015, **31**, 1605–1609.
34 L. Deng, S.-F. Hung, Z.-Y. Lin, Y. Zhang, C. Zhang, Y. Hao, S. Liu, C.-H. Kuo, H.-Y. Chen, J. Peng, J. Wang and S. Peng, Valence Oscillation of Ru Active Sites for Efficient and Robust Acidic Water Oxidation, *Adv. Mater.*, 2023, 2305939.
35 X. Zhang, L. Xia, G. Zhao, B. Zhang, Y. Chen, J. Chen, M. Gao, Y. Jiang, Y. Liu, H. Pan and W. Sun, Fast and Durable Alkaline Hydrogen Oxidation Reaction at the Electron-Deficient Ruthenium–Ruthenium Oxide Interface, *Adv. Mater.*, 2023, **35**, 2208821.
36 J. Peng, Y. Chen, K. Wang, Z. Tang and S. Chen, High-performance Ru-based electrocatalyst composed of Ru nanoparticles and Ru single atoms for hydrogen evolution reaction in alkaline solution, *Int. J. Hydrogen Energy*, 2020, **45**, 18840–18849.
37 C. Bock, C. Paquet, M. Couillard, G. A. Botton and B. R. MacDougall, Size-Selected Synthesis of PtRu Nano-Catalysts: Reaction and Size Control Mechanism, *J. Am. Chem. Soc.*, 2004, **126**, 8028–8037.
38 Y. Qin and X. Bai, Hydrogenation of N-ethylcarbazole over Ni-Ru alloy nanoparticles loaded on graphitized carbon prepared by carbothermal reduction, *Fuel*, 2022, **307**, 121921.
39 S. H. Ahn, O. J. Kwon, S.-K. Kim, I. Choi and J. J. Kim, Electrochemical preparation of Pt-based ternary alloy catalyst for direct methanol fuel cell anode, *Int. J. Hydrogen Energy*, 2010, **35**, 13309–13316.
40 M. A. Sabri, G. Bharath, A. Hai, M. A. Haija, R. P. Nogueira and F. Banat, Highly efficient PdNiB decorated over carbon supports for the electrochemical valorization of furfural and 5-hydroxymethylfurfural into fuels, *Fuel*, 2023, **353**, 129241.
41 X. Huang, L. Zhang, C. Li, L. Tan and Z. Wei, High Selective Electrochemical Hydrogenation of Cinnamaldehyde to Cinnamyl Alcohol on RuO_2–SnO_2–TiO_2/Ti Electrode, *ACS Catal.*, 2019, **9**, 11307–11316.
42 D. Zhang, J. Chen, Z. Hao, L. Jiao, Q. Ge, W.-F. Fu and X.-J. Lv, Highly efficient electrochemical hydrogenation of acetonitrile to ethylamine for primary amine synthesis and promising hydrogen storage, *Chem Catal.*, 2021, **1**, 393–406.
43 K. Ji, M. Xu, S.-M. Xu, Y. Wang, R. Ge, X. Hu, X. Sun and H. Duan, Electrocatalytic Hydrogenation of 5-Hydroxymethylfurfural Promoted by a Ru1Cu Single-Atom Alloy Catalyst, *Angew. Chem., Int. Ed.*, 2022, **61**, e202209849.
44 X.-Q. Pan, X.-Y. Zhang, G.-X. Huang, S.-C. Mei, J.-W. Huang, J.-J. Chen, W.-J. Liu and H.-Q. Yu, Promoting electrocatalytic hydrogenation of 5-hydroxymethylfurfural using buffer electrolytes as proton-donating motifs: theoretical predictions and experimental validations, *Appl. Catal., B*, 2023, **323**, 122191.
45 L. Zhou, Y. Li, Y. Lu, S. Wang and Y. Zou, pH-Induced selective electrocatalytic hydrogenation of furfural on Cu electrodes, *Chin. J. Catal.*, 2022, **43**, 3142–3153.

46 N. F. L. Machado, M. P. M. Marques, L. A. E. Batista de Carvalho, J. L. Castro and J. C. Otero, Anomalous surface-enhanced Raman scattering of aromatic aldehydes and carboxylic acids, *J. Raman Spectrosc.*, 2017, **48**, 413–417.

47 W. Xi and A. J. Haes, Elucidation of pH impacts on monosubstituted benzene derivatives using normal Raman and surface-enhanced Raman scattering, *J. Chem. Phys.*, 2020, **153**, 184707.